Connecting the Tropics to the Polar Regions — SPECIAL COLLECTION

Stationary Wave Interference and Its Relation to Tropical Convection and Arctic Warming

MICHAEL GOSS AND STEVEN B. FELDSTEIN

Department of Meteorology, The Pennsylvania State University, University Park, Pennsylvania

SUKYOUNG LEE

Department of Meteorology, The Pennsylvania State University, University Park, Pennsylvania, and School of Earth and Environmental Sciences, Seoul National University, Seoul, South Korea

ABSTRACT

The interference between transient eddies and climatological stationary eddies in the Northern Hemisphere is investigated. The amplitude and sign of the interference is represented by the stationary wave index (SWI), which is calculated by projecting the daily 300-hPa streamfunction anomaly field onto the 300-hPa climatological stationary wave. ERA-Interim data for the years 1979 to 2013 are used. The amplitude of the interference peaks during boreal winter. The evolution of outgoing longwave radiation, Arctic temperature, 300-hPa streamfunction, 10-hPa zonal wind, Arctic sea ice concentration, and the Arctic Oscillation (AO) index are examined for days of large SWI values during the winter.

Constructive interference during winter tends to occur about one week after enhanced warm pool convection and is followed by an increase in Arctic surface air temperature along with a reduction of sea ice in the Barents and Kara Seas. The warming of the Arctic does occur without prior warm pool convection, but it is enhanced and prolonged when constructive interference occurs in concert with enhanced warm pool convection. This is followed two weeks later by a weakening of the stratospheric polar vortex and a decline of the AO. All of these associations are reversed in the case of destructive interference. Potential climate change implications are briefly discussed.

1. Introduction

The Northern Hemispheric climatological stationary wave is a primarily low zonal wavenumber feature in the flow that is likely the result of a complex interplay between thermal and orographic forcing in both the tropics and extratropics (e.g., Held et al. 2002). Recent studies have shown that important insights about the dynamics of the Northern Hemispheric circulation can be gleaned by investigating the role of transient eddy interference with the climatological stationary wave, including insights into tropical–extratropical interactions (Fletcher and Kushner 2011; Garfinkel et al. 2012), potential connections to global warming (Lee 2014), Arctic sea ice loss (Peings and Magnusdottir 2014; Kim et al. 2014; Feldstein and Lee 2014), and the stratospheric polar vortex (Limpasuvan and Hartmann 2000; Cohen et al. 2007; Garfinkel et al. 2010; Fletcher and Kushner 2011; Smith et al. 2011).

Tropical convective forcing is known to excite a Rossby wave response in the extratropics of the Northern Hemisphere (e.g., Hoskins and Karoly 1981; Simmons 1982; Sardeshmukh and Hoskins 1988). Tropical convective heating can therefore comprise a significant component of the stationary wave forcing (Held et al. 2002). In addition, recent studies (Lee et al. 2011a,b; Yoo et al. 2012a,b; Baggett and Lee 2015) have indicated a link between localized tropical convective forcing and changes in Arctic surface air temperature (SAT). There are other studies that link tropical sea surface temperature anomalies to changes in Arctic SAT (Lee 2012; Ding et al. 2014). These studies have shown that the tropical heating excites poleward Rossby wave propagation that drives changes in Arctic SAT through its influence on high-latitude downward infrared radiation (IR), horizontal temperature advection, and adiabatic warming/cooling. Intuitively, it would not

be surprising if anomalous tropical convection were to excite transient eddies, which constructively or destructively interfere with the climatological stationary wave, with the resulting amplification or deamplification of the extratropical flow resulting in more or less heat and moisture (which can change the downward IR) transport into the Arctic, leading to changes in both the Arctic SAT and Arctic sea ice (Henderson et al. 2014; Lee 2014; Park et al. 2015).

Several recent studies (Cohen et al. 2007, 2014) have shown a link between snow cover anomalies over Eurasia and planetary wave propagation into the stratosphere, altering the stratospheric polar vortex and influencing the Arctic Oscillation [AO; or, alternatively, the lower-tropospheric realization of the Northern Annular Mode (NAM)]. The role of the climatological stationary wave in modulating this process is discussed in Smith et al. (2011), where it is argued that planetary wave propagation into the stratosphere strongly depends on the presence of constructive interference with the stationary wave. Other recent studies have shown a connection between interference and the strength of the stratospheric polar vortex that appears to be triggered by tropical convection associated with El Niño–Southern Oscillation (ENSO) (Fletcher and Kushner 2011) and the Madden–Julian oscillation (MJO; Garfinkel et al. 2012). These studies find that poleward-propagating planetary-scale Rossby waves excited by tropical convection can constructively or destructively interfere with the climatological stationary wave field, which alters the strength of the stratospheric polar vortex via changes in the amplitude of the vertical propagation of planetary waves into the stratosphere.

With the above in mind, we will use observational data to study questions related to transient eddy interference with the wintertime Northern Hemispheric climatological stationary wave as it relates to the extratropical circulation, tropical convection, Arctic surface temperature, sea ice, and the stratospheric polar vortex. Specifically, we seek to address the following key questions: 1) How does the structure and amplitude of the wave field vary throughout the course of the year when there is interference between transient eddies and the climatological stationary wave? 2) Is an enhancement of tropical convective heating associated with constructive transient eddy interference with the climatological stationary wave? 3) Is constructive interference in winter associated with warmer Arctic surface temperatures? 4) If there is an association between interference and the Arctic surface temperature, is this association modulated by tropical convection?

In section 2, we discuss the data and methods used in this study. We present the major results of the study in section 3. Finally, in section 4, we discuss the results in the context of the questions posed above and make a few concluding remarks.

2. Data and methods

For this study, ERA-Interim data are used for all variables unless otherwise stated, for the period 1979–2013 and with a grid spacing of $1.5° \times 1.5°$. To quantify the amplitude of the transient interference with the Northern Hemisphere climatological stationary wave, a daily stationary wave index (SWI) is calculated using the following method. For each grid point, the climatological annual cycle of the 300-hPa streamfunction field is determined by first calculating the mean of the 35 values of 300-hPa streamfunction for each day of the year. Applying a low-pass temporal filter at each grid point, the first 10 harmonics of the annual cycle are retained to retrieve a smoothed climatology $\overline{\Psi}$. For each day of the year, the zonal mean of the smoothed climatology $[\overline{\Psi}]$ is subtracted at each grid point. The result is the 300-hPa climatological stationary wave $\overline{\Psi^*}$ for each day of the year.

Next, the daily 300-hPa streamfunction anomalies are calculated at each grid point by subtracting $\overline{\Psi}$ for the corresponding day of the year from the daily streamfunction Ψ. We label the resulting daily 300-hPa streamfunction anomaly field as Ψ'. The daily anomaly field is then projected onto the climatological stationary wave for the corresponding day of the year:

$$P(t) = \frac{\sum_i \sum_j \Psi'(\lambda_i, \theta_j, t)\overline{\Psi^*}(\lambda_i, \theta_j, d)\cos\theta}{\sum_i \sum_j [\overline{\Psi^*}(\lambda_i, \theta_j, d)]^2 \cos\theta}. \quad (1)$$

Here, $P(t)$ is the projection for a given date t, d is the day of the year corresponding to t, λ_i is the longitude at zonal grid point i, and θ_j is the latitude at meridional grid point j. We perform this calculation at all longitudes, for latitudes between 15° and 75°N. This latitudinal domain is chosen to capture the variability in the amplitude of Northern Hemispheric stationary wave. Alternative near-hemispheric latitudinal domains were tested, and the results were found to be largely insensitive to the exact latitude bounds chosen. Finally, the daily SWI is calculated by normalizing $P(t)$—specifically, for each day, the mean value of $P(t)$ is subtracted, and the result is divided by the standard deviation of $P(t)$.

To study how interference with the climatological stationary wave depends on zonal wavenumber, an identical analysis is performed using (1), but for which Ψ' and $\overline{\Psi^*}$ have first been filtered by individual zonal wavenumber, ranging from 1 to 3. The resulting $P(t)$ values are again normalized by their mean and standard

TABLE 1. Number of DJF days in each composite, based on the criteria in the left column. The OLR index is based on the lag day −10 to 0 warm pool OLR (see text for details).

Criteria		Number of days
All DJF days		3159
$SWI > 1.0$	All	375
$SWI > 1.0$	$OLR > 0.5$	64
$SWI > 1.0$	$-0.5 \leq OLR \leq 0.5$	94
$SWI > 1.0$	$OLR < -0.5$	217
$SWI < -1.0$	All	371
$SWI < -1.0$	$OLR > 0.5$	182
$SWI < -1.0$	$-0.5 \leq OLR \leq 0.5$	82
$SWI < -1.0$	$OLR < -0.5$	106
$SWI_1 > 1.0$		300
$SWI_1 < -1.0$		333
$SWI_2 > 1.0$		520
$SWI_2 < -1.0$		546
$SWI_3 > 1.0$		310
$SWI_3 < -1.0$		311

deviation to retrieve SWI time series for each zonal wavenumber. These time series are designated as SWI_1 through SWI_3. (We focus on wavenumbers 1 through 3 because it is these wavenumbers that account for the largest contribution to the climatological stationary wave.)

Lagged composites of several atmospheric variables and indices are calculated for those days when there is large amplitude constructive or destructive inference. (The number of days in each composite seen in this study is found in Table 1.) Specifically, daily anomalies of outgoing longwave radiation (OLR), 2-m temperature, sea ice concentration, and 10-hPa zonal wind are calculated in the same manner as the 300-hPa stream-function anomalies. That is, a smoothed climatological annual cycle is first calculated at each grid point for each variable. The anomalies are calculated by subtracting the smoothed climatology for the corresponding day of the year. The Arctic Oscillation (AO) index is obtained from the National Oceanic and Atmospheric Administration's Climate Prediction Center (NOAA/CPC). For the composites, lag day zero corresponds to December through February (DJF) days during which transient interference with the climatological stationary wave is constructive ($SWI > 1.0$) or destructive ($SWI < -1.0$).

To address questions of causal processes, for the above variables, statistical significance is determined using a Monte Carlo simulation at the (two-tailed) $p < 0.05$ level. Specifically, at each grid point for each lag day, 10 000 randomly chosen pairs of subsamples of the variable are produced using the subset of days from which the lag day in question could potentially draw [e.g., for lag day 0 (DJF) or for lag day −30

(1 November through 30 January)]. The number of random days chosen per subsample is the number of days that go into the composite divided by the average number of consecutive days, during DJF, for which the SWI falls above the 1.0 (constructive) or below the −1.0 (destructive) value threshold. The resulting value is rounded to the nearest integer. For example, there are 361 DJF days for which the SWI is greater than 1.0, and on average the SWI exceeds 1.0 for 3.38 consecutive days. Therefore, the constructive interference subsamples in the lag day 0 case are made up of $361/3.38 \approx 107$ randomly chosen days from DJF. The 10 000 mean values of the random destructive interference subsamples are subtracted from the 10 000 mean values of the random constructive interference subsamples. Finally, these differences are sorted at each grid point. Any grid point for which the difference between the constructive composite value and the destructive composite value falls outside of the middle 95% of subsample mean differences for that grid point is considered statistically significant. Finally, for the sea ice concentration composite, statistical significance is evaluated only for those locations in which the absolute difference between the composite sea ice concentration values in the constructive and destructive cases is greater than 0.1%, in order to neglect fluctuations in regions with near-100% ice cover.

Finally, in order to test the sensitivity to determining composites based on all days for which the threshold value of 1.0 or −1.0 is exceeded, which leads to consecutive days from one event being considered a "day 0" for the composite, versus calculating composites based on individual events, we recalculate the composites in each figure using the following method to choose composite days. First, we choose the highest SWI value during DJF and assign that day as lag day 0 for event number 1. Next, we block out that day and the 3 days on either side of that event so that those days cannot be considered for the composite on future iterations. The next highest available DJF day is then selected as lag day 0 for event number 2, again blocking out that day and the 3 days on either side from future consideration. This process is repeated until the top 50 events are found, and the composite of those 50 days is used. The Monte Carlo test described above is used to calculate statistical significance, but since each event is separated by at least 6 days, we use exactly 50 randomly selected days for each composite. The results of this sensitivity test are not shown; however, we find that the qualitative results are unchanged, the conclusions drawn from them are the same, and the statistical significance is almost identical. We choose the threshold method in this study because of the good match with the events method in the statistical

tests and because the results, not unexpectedly, appear smoother than with the events method.

3. Results

To visualize the transient wave field associated with the SWI, we calculate composites of the 300-hPa total streamfunction (Ψ, black contours) and 300-hPa streamfunction anomalies (Ψ′, shading), first for constructive interference and again for destructive interference. Composites are calculated for days from all months and separately for each meteorological season, as shown in Fig. 1. We see that the largest-amplitude anomalies occur in the winter months and that the anomaly centers are similar from autumn through spring. The constructive interference composite in those seasons is associated with large positive Ψ′ values over the northeastern North Pacific and western North America, over the northeastern North Atlantic through Scandinavia, and over the northwestern subtropical Pacific. Large negative Ψ′ values are found over northeastern North America, the northwestern North Pacific, the northeastern subtropical Pacific, and from the northeastern subtropical Atlantic through the Mediterranean. Opposite-signed Ψ′ values are found in the destructive interference composites. The Ψ contours illustrate amplification of the climatological stationary eddy field when there is constructive interference and a flow that is nearly zonal when there is destructive interference. The summer composites show a much weaker, less organized anomaly pattern. The winter pattern is the focus of this study.

The time evolution of the anomalous 300-hPa streamfunction field is shown in Fig. 2. Most notably, positive (negative) 300-hPa streamfunction anomalies are found at high latitudes following days with constructive (destructive) transient wave interference with the climatological stationary wave. The location and westward propagation of the positive streamfunction anomaly resembles that of the positive sea level pressure (SLP) anomaly found in Cohen and Jones (2011) prior to stratospheric polar vortex displacements. Lagged composites for OLR are shown in Fig. 3. We note that constructive (destructive) interference is preceded by a tripole pattern of enhanced (suppressed) convection over the Maritime Continent, flanked on either side by regions of suppressed (enhanced) convection over the equatorial Indian Ocean and central equatorial Pacific Ocean. These anomalies have characteristics of both MJO phase 5 (1) of Wheeler and Hendon (2004) and La Niña (El Niño) for constructive (destructive) interference. In Fig. 4, we show lagged composites of Arctic 2-m temperature. Here, for the constructive

(destructive) interference case, it is seen that there are positive (negative) temperature anomalies, which are first observed over Siberia and then over Alaska, that spread poleward, warming (cooling) most of the Arctic at positive lags. Prior to lag day −6 (not shown), the spatial pattern of the SAT anomalies remains essentially unchanged, with the warm (cold) anomaly over Siberia and the Barents and Kara Seas region seen all the way back to lag day −25 (lag day −20). In Fig. 5, lagged composites of Arctic sea ice concentration are shown. We see that constructive (destructive) interference is associated with persistently negative (positive) sea ice concentration anomalies over the Barents and Kara Seas, with the opposite-signed anomalies found in the Canadian Archipelago. In both cases, these anomalies begin to appear near lag day −12 and increase in amplitude through lag day 0, remaining strong through lag day +20. Finally, in Fig. 6, we show lagged composites of the 10-hPa zonal wind. As can be seen, in the case of constructive interference, although the stratospheric polar vortex at negative lags is initially stronger than normal, as illustrated by the positive zonal wind anomalies at most longitudes near 60°N, these anomalies quickly deteriorate and, in many locations, become negative at positive lags. This suggests a weakening of the stratospheric polar vortex coinciding with and following constructive interference. The opposite, a strengthening of the vortex, is seen during and following destructive interference.

To more easily interpret the above lagged composites, we introduce indices that capture the essential features of the variables of interest. Specifically, indices are calculated to approximate warm pool convection using OLR, Arctic SAT anomalies, Barents and Kara Sea ice coverage using sea ice concentration, and the strength of the stratospheric polar vortex using the 10-hPa zonal wind. For the warm pool convection index, we take the mean OLR anomaly value in a box that extends from 15°S to 15°N latitude and from 90°E to 150°E longitude. A second warm pool convection index is calculated in the same manner, except that a 180-day high-pass filter is then applied to the time series in order to filter out longer time-scale variability, such as that associated with ENSO. The Arctic SAT index is calculated as the area-weighted mean 2-m temperature poleward of 70°N. The Barents and Kara Sea ice coverage index is created by taking an area-weighted mean of the sea ice concentration anomalies over the region extending from 70° to 80°N and from 30° to 75°E. A 180-day high-pass filter is applied to the resulting time series in order to remove variability associated with the long-term interdecadal sea ice trend. Finally, the stratospheric polar vortex strength is approximated with an index that is calculated
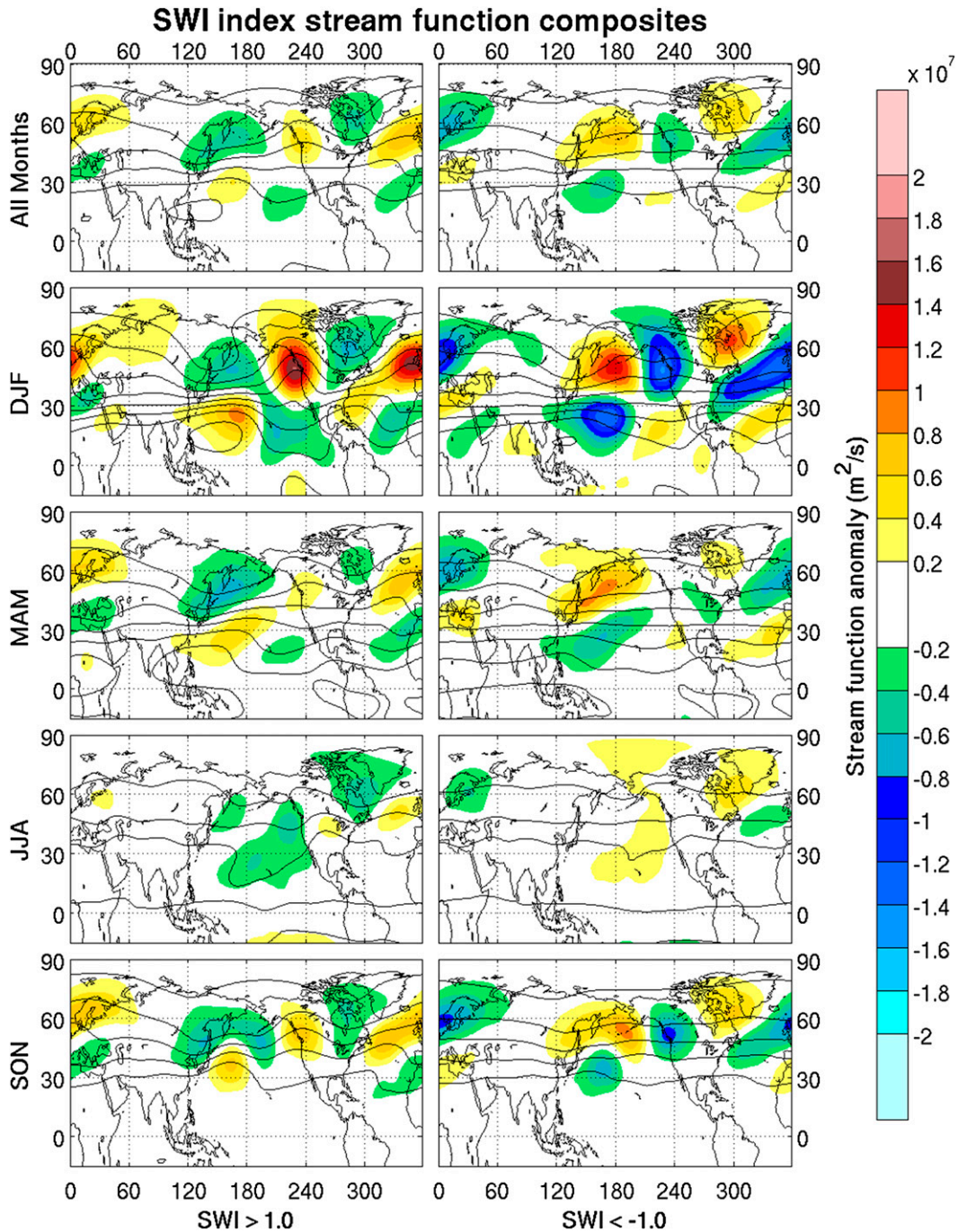
SWI index stream function composites

FIG. 1. Composite 300-hPa streamfunction anomaly maps for days with (left) SWI > 1.0 and (right) SWI < −1.0; days are from (top to bottom) all seasons, December–February, March–May, June–August, and September–November. Contours correspond to the composite total 300-hPa streamfunction for the same days, with a contour interval of $20 \times 10^6\,\mathrm{m}^2\,\mathrm{s}^{-1}$.

by taking the zonal mean of the 10-hPa zonal wind at 60°N.

In Fig. 7, lagged composites based on high SWI values (constructive interference) and low SWI values (destructive interference) are shown. The variables plotted

are the indices described above, in addition to the SWI itself, and the AO. We examine the AO because many previous studies have shown that anomalies in the stratospheric zonal wind are followed by anomalies at the surface corresponding to the AO (e.g., Baldwin and
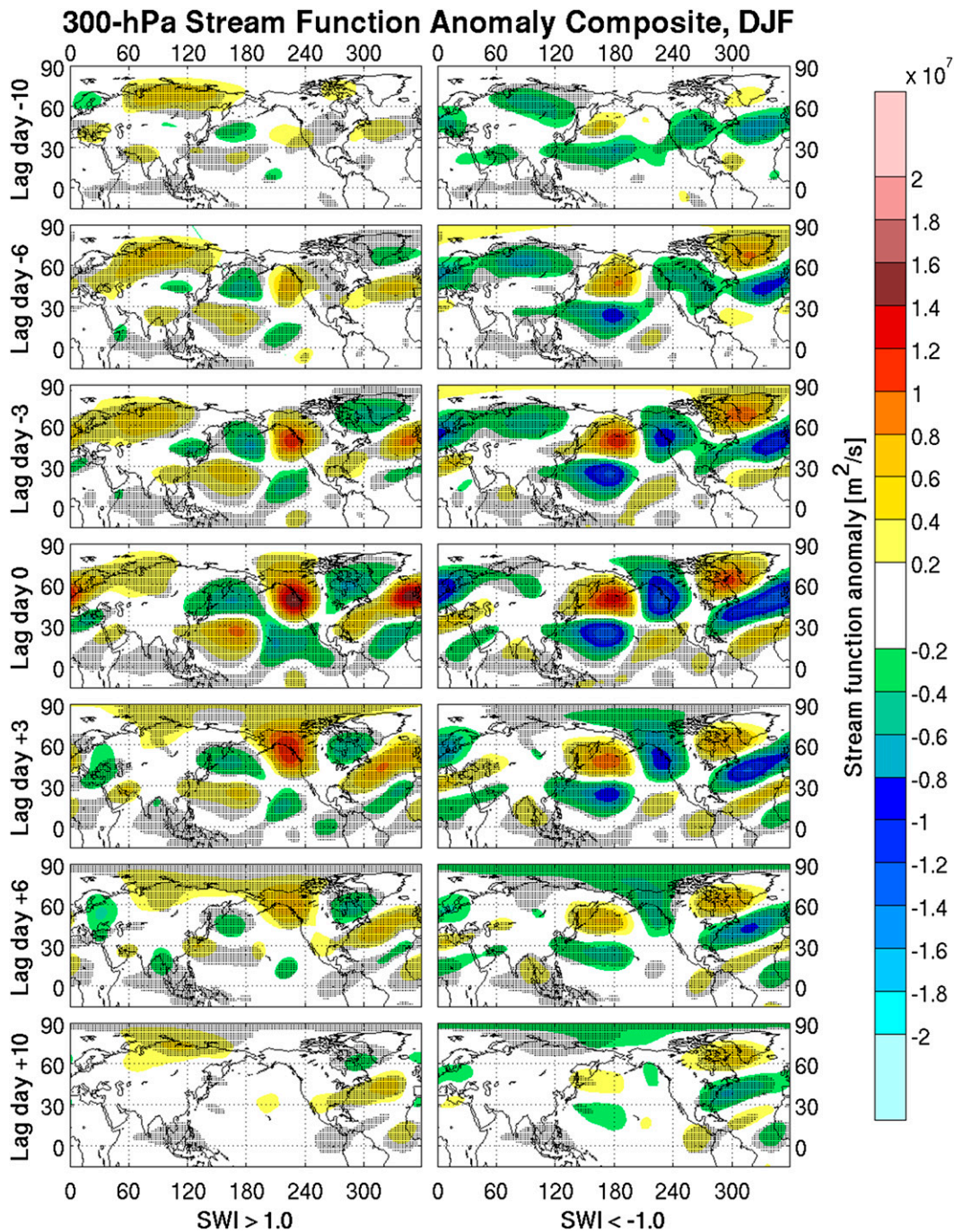
300-hPa Stream Function Anomaly Composite, DJF

FIG. 2. Lagged composite 300-hPa streamfunction anomaly maps for DJF days with (left) SWI > 1.0 and (right) SWI < −1.0. The rows correspond to (top to bottom) lag −10, −6, −3, 0, +3, +6, and +10 days. Stippling indicates regions where the left- and right-column composites are statistically different at the $p < 0.05$ level, according to a Monte Carlo simulation (see text for details).

Dunkerton 1999, 2001; Gillett et al. 2001; Thompson et al. 2002; Charlton et al. 2003). Statistical significance at the (two-tailed) $p < 0.05$ level in Fig. 7 is shown with thick lines and is determined using a similar Monte Carlo simulation as described in section 2. However,

instead of testing whether there is a statistically significant difference between the constructive and destructive cases, here we simply test, individually for the constructive and destructive interference cases, whether the mean index value itself is statistically significant.
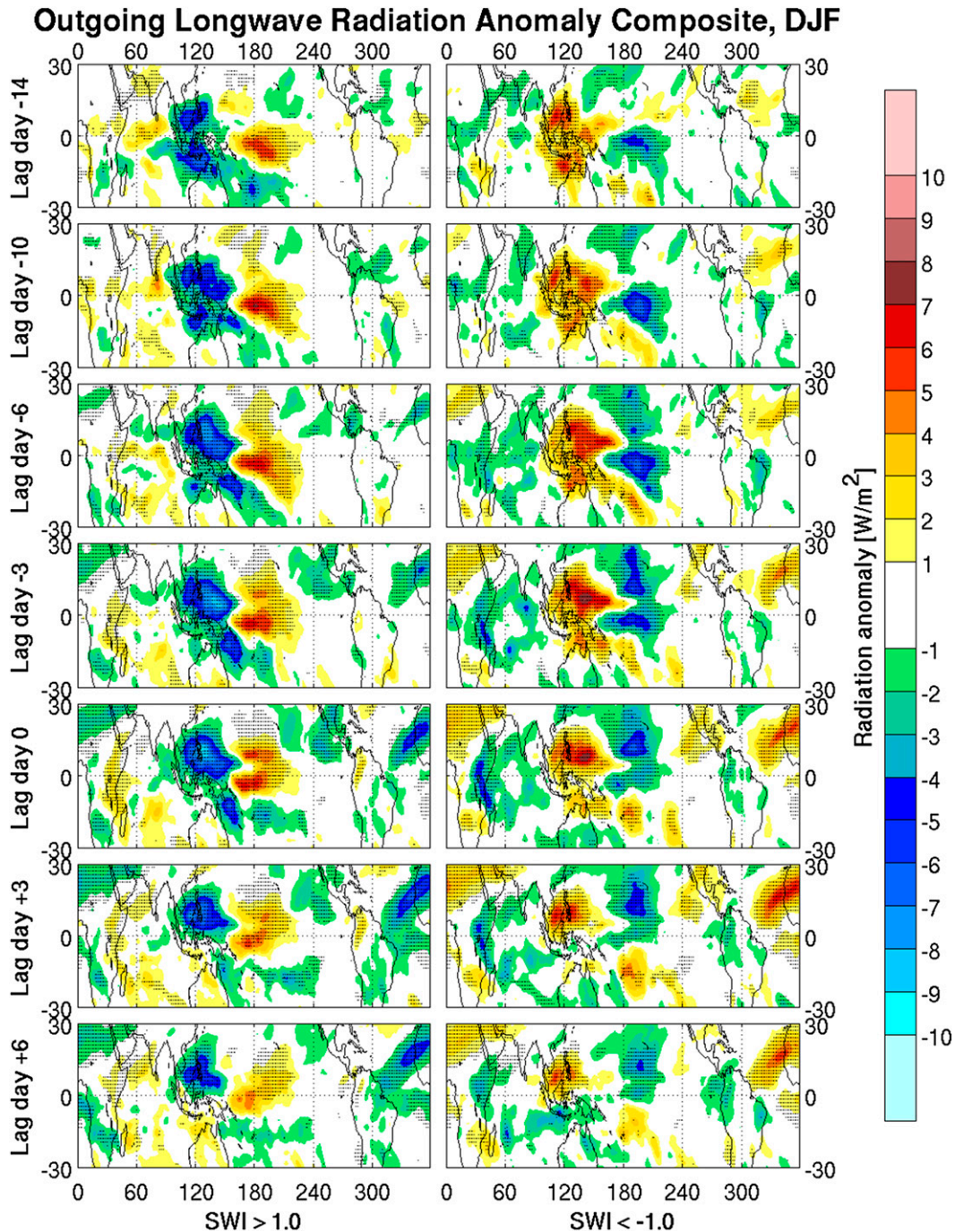
Outgoing Longwave Radiation Anomaly Composite, DJF

FIG. 3. As in Fig. 2, but for anomalous outgoing longwave radiation and for the rows corresponding to (top to bottom) lag −14, −10, −6, −3, 0, +3, and +6 days.

Therefore, the mean values of the 10 000 random sub-samples are sorted independently for the constructive and destructive interference cases, and any composite value for the given case that falls outside of the middle 95% of subsample means for that case is considered statistically significant.

The results in Fig. 7 suggest that constructive interference is preceded (at approximately lag days −20 to 0) by enhanced warm pool convection (Fig. 7, top). A warm Arctic SAT signal is found at lag days −17 to +17, peaking at lag day +8. From approximately lag days −15 to +15, the sea ice anomaly in the Barents and
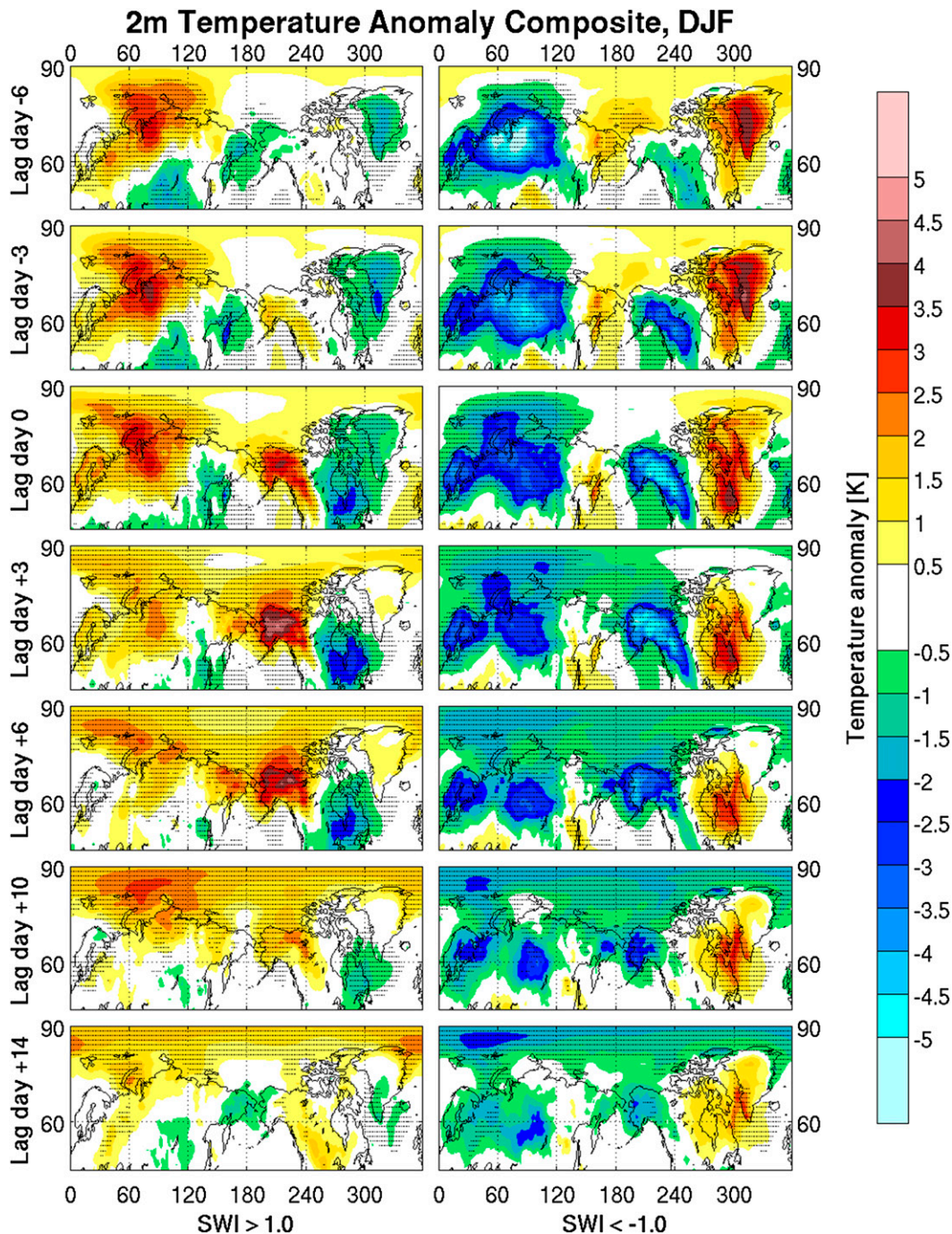
FIG. 4. As in Fig. 2, but for anomalous 2-m temperatures and for the rows corresponding to (top to bottom) lag −6, −3, 0, +3, +6, +10, and +14 days.

Kara Seas is weakly negative. Although none of the sea ice values shown exceed the $p < 0.05$ threshold, they do at the $p < 0.10$ threshold for lag days −3 to +3 (not shown). The warm SAT signal over the Barents and Kara Seas at negative lags (Fig. 4; described above for earlier lags) is consistent with the low sea ice

concentration over the same region. In addition, the AO is seen to have a positive peak at lag day 0 with values satisfying the $p < 0.05$ threshold from lag days −3 to +3. The stratosphere is anomalously strong prior to constructive interference and then weakens substantially to a point where it is no longer significantly positive by
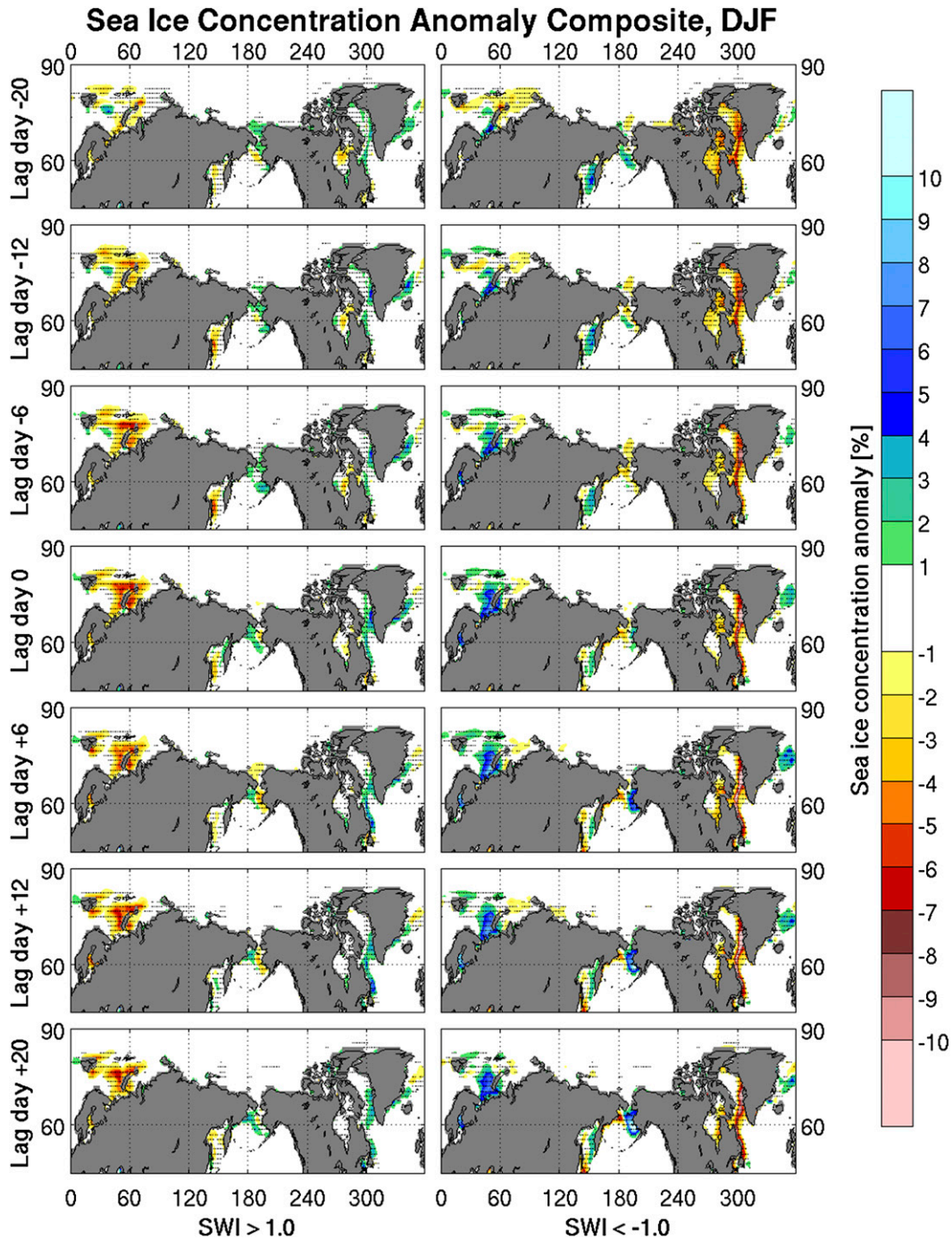
FIG. 5. As in Fig. 2, but for anomalous sea ice concentration and for the rows corresponding to (top to bottom) lag −20, −12, −6, 0, +6, +12, and +20 days, respectively.

lag day 0 and beyond. Destructive interference shows many of the same features but of the opposite sign (Fig. 7, bottom). For example, a negative SWI is preceded, at similar lag days, by suppressed warm pool convection. There is a cold Arctic SAT signal from lag days +2 to +12, peaking at lag day +5. In contrast to the

constructive interference case, the signal for higher-than-normal Barents and Kara Sea ice shows $p < 0.05$ values associated with destructive interference that extend from lag days −19 to +7. The anomalously high concentration of Barents and Kara Sea ice at negative lags is consistent with the cold SAT anomalies seen over

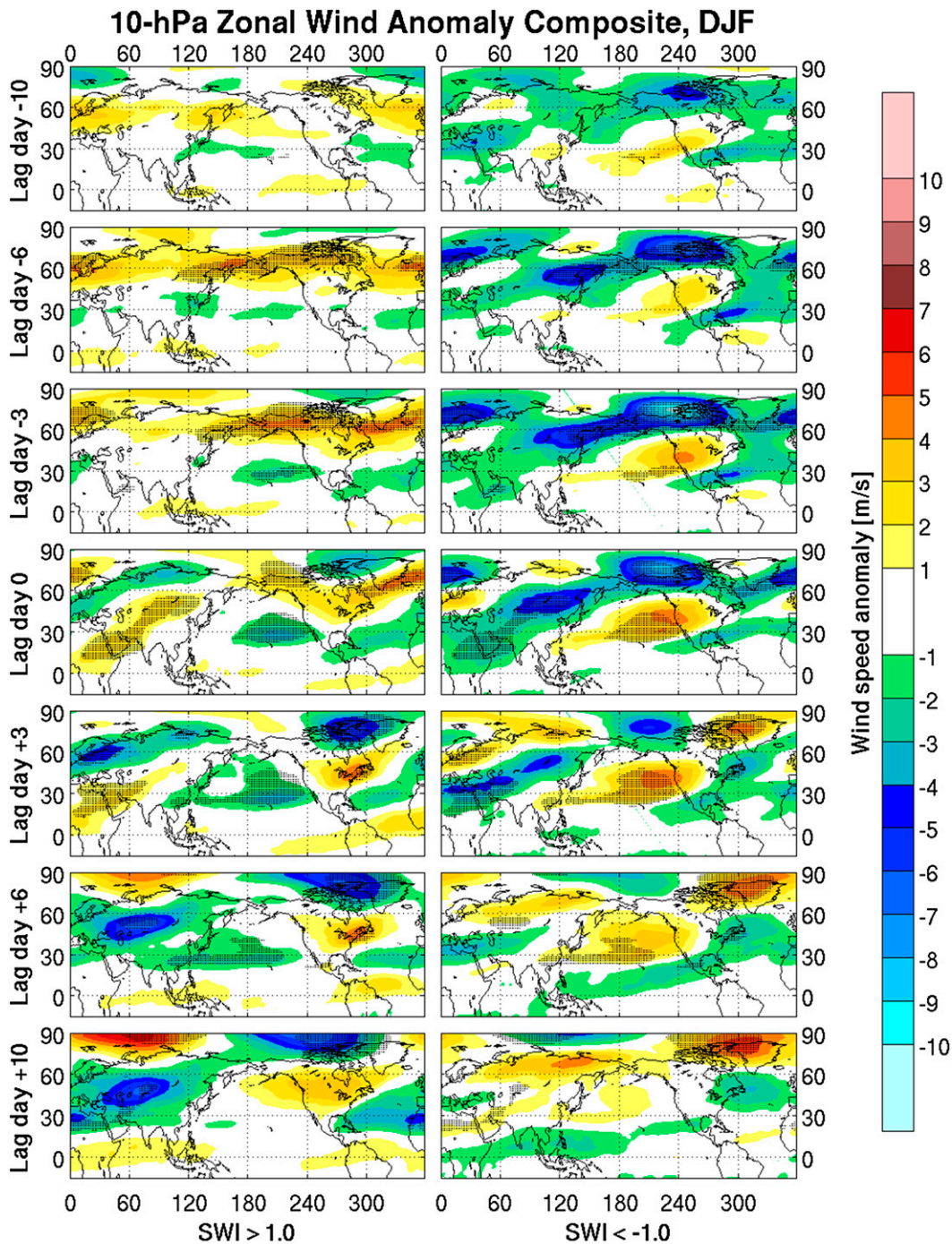## 10-hPa Zonal Wind Anomaly Composite, DJF

FIG. 6. As in Fig. 2, but for the anomalous 10-hPa zonal wind.

the same region at negative lags (Fig. 4; described above for earlier lags). The AO is seen to have a negative peak near the same time as the peak in destructive interference that exceeds the $p < 0.05$ threshold for a larger number of days than when there is constructive interference, ranging from lag days −29 to +11. Finally, although not statistically significant, there is a hint that

the stratospheric polar vortex is weakened prior to destructive interference and strengthened during and after the period of destructive interference.

For the constructive interference case, there is also a signal for higher-than-normal concentrations of sea ice in the Barents and Kara Seas at much earlier times, ranging approximately from lag days −50 to −25.
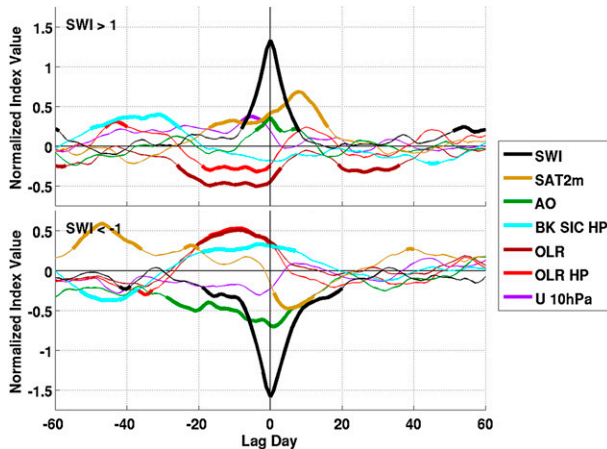
FIG. 7. Lagged composite plots of normalized indices for DJF days with (top) SWI > 1.0 and (bottom) SWI < −1.0. The black curve corresponds to the SWI, the gold curve to 2-m temperatures poleward of 70°N, the green curve to the Arctic Oscillation index, and the cyan curve to the anomalous sea ice concentration in the Barents and Kara Seas, with a 180-day high-pass filter applied. The dark red curve corresponds to the anomalous outgoing longwave radiation over the warm pool region, the bright red curve is the same variable but with a 180-day high-pass filter applied, and the purple curve corresponds to the anomalous 10-hPa zonal mean zonal wind at 60°N. Thick lines correspond to lag days for which the composite value is statistically significant at the $p < 0.05$ level according to a Monte Carlo simulation (see text for details).

Similarly, lower-than-normal concentrations of sea ice in the Barents and Kara Seas are found at lag days −55 to −35 prior to the destructive interference case. The statistically significant signal at negative lags may suggest the possibility that the sea ice concentration in the Barents and Kara Seas preconditions the atmosphere in some way to favor the development of constructive or destructive interference with the climatological stationary wave. To examine this possibility further, we reproduce Fig. 7 two additional times, compositing against the Barents and Kara Sea ice index and the 10-hPa zonal mean zonal wind index, and investigate the resulting SWI signal (the results are not shown). For the Barents and Kara Sea ice, we do not find a statistically significant SWI signal at positive lags, although the sign of the SWI is consistent with that shown in Fig. 7. For the stratospheric polar vortex, there is a statistically significant SWI signal at positive lags consistent with that seen in Fig. 7. However, the composite SWI is barely statistically significant and for a very short time window. These results suggest that while preconditioning may be a factor in inducing stationary wave interference (especially for the stratospheric polar vortex), it is likely not the key factor.

Figure 8 shows lag day 0 composites of Ψ' (color) and $\overline{\Psi^*}$ (black contours; the climatological stationary eddies

for zonal wavenumbers 1 to 3), based on positive and negative SWI_1–SWI_3 values during DJF. In the SWI_1 case, constructive interference (Fig. 8, left) is associated most strongly with positive Ψ' values over northeastern North America that extend eastward to western Siberia and from southeastern Asia to just north of Hawaii. Negative Ψ' values are found from central Asia to the Aleutian Islands and from the subtropical North Atlantic to the Mediterranean. For the SWI_2 and SWI_3 composites during times of constructive interference, a high-amplitude positive Ψ' center is found over Alaska and the northeastern North Pacific, with negative anomalies centered over northeastern North America. The anomalies over the eastern North Atlantic and much of Eurasia are of opposite signs between SWI_2 and SWI_3. The former shows positive anomalies to the south of the Azores, as well as over Scandinavia and western Russia, with negative anomalies centered south of Iceland and over Lake Baikal. The SWI_3 case shows opposite-signed anomalies over those same regions. For each of the SWI_1–SWI_3 cases, the destructive interference composites (Fig. 8, right) show opposite-signed anomalies compared to the constructive interference composites. It is seen that the Ψ' composite anomalies align quite well with $\overline{\Psi^*}$, indicating the presence of interference separately for each wavenumber. Additionally, a qualitative inspection of SWI_1–SWI_3 shows that the SWI can be approximated as the superposition of the SWI_1–SWI_3.

Figure 9 is analogous to Fig. 7, except that instead of compositing against the SWI, the composites are based on positive and negative SWI_1–SWI_3 values. Constructive interference in the SWI_1 case (Fig. 9, top left) is preceded more than 40 days earlier by an enhanced stratospheric polar vortex, increased Barents and Kara Sea ice, a positive AO, and then by enhanced warm pool convection beginning at lag −17 days. The association with the Arctic SAT is much weaker than with the +SWI, with a significant peak warming occurring at lag day −7 and another barely significant peak at lag day +23. The peak in constructive interference occurs at about the same time as the statistically significant decrease in Barents and Kara Sea ice with $p < 0.05$ values from lag days −10 to +18. Following the peak in constructive interference, the stratospheric polar vortex becomes significantly weaker than normal, with $p < 0.05$ values extending from lag days +14 to +47. The constructive interference is also followed by a marginally negative AO with $p < 0.05$ values for lag +15 to +18 days and lag +22 to +24 days. The destructive interference case shows largely the opposite signals (Fig. 9, top right), although the negative Arctic SAT signal and the positive AO signal at positive lags are not
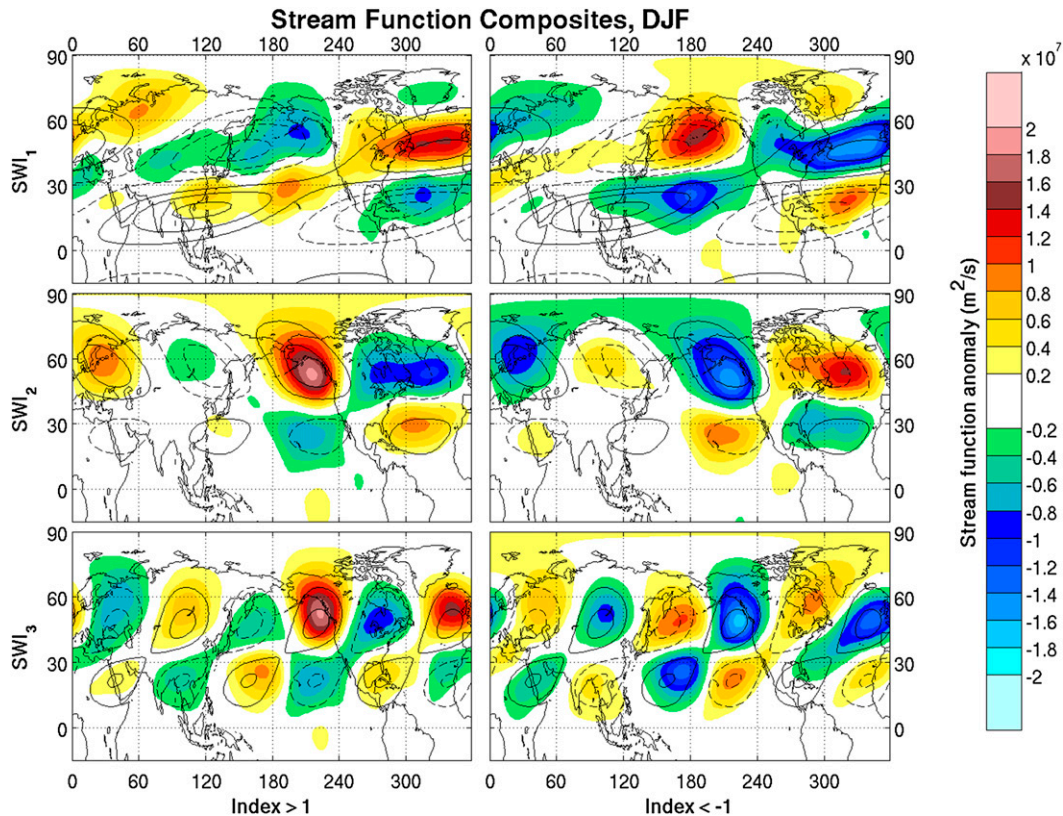
FIG. 8. Composite 300-hPa streamfunction anomaly maps for DJF days with (left) constructive (index > 1.0) and (right) destructive (index < −1.0) interference. Composites are based on (top to bottom) SWI_1, SWI_2, and SWI_3 (see text). Contours correspond to the DJF 300-hPa climatological stationary wave $\overline{\Psi^*}$ for the corresponding zonal wavenumber. The contour interval is $4 \times 10^6 \, m^2 \, s^{-1}$, with the zero contour not plotted, positive anomalies plotted as solid contours, and negative anomalies as dashed contours.

significant. Additionally, lagged composite plots of SLP at positive lags (not shown) demonstrate weak positive (negative) SLP anomalies over the pole and negative (positive) SLP anomalies over the North Pacific and North Atlantic, at lag +20 to +50 days for the positive (negative) SWI_1, consistent with the AO signal seen in Fig. 9. The AO signal may also be seen as a response to the SAT changes associated with the SWI_1, with warming being associated with the negative AO and cooling with the positive AO. However, the AO response to the SWI_1 tends to occur at later lags than the peak Arctic SAT anomaly. Although warming (cooling) of the Arctic may contribute to the excitation of the negative (positive) AO, because of these time lags, it seems more likely that the weakening (strengthening) of the stratospheric polar vortex is the key factor in driving the negative (positive) AO.

As with the results from Fig. 7, the high and low SWI_1 composites show signals at negative lags for several variables. Specifically, it is seen that Barents and Kara Sea ice concentration is higher than average at lag

days −54 to −25, the stratospheric polar vortex is stronger than average at lag days −47 to −2, and the AO index is higher than average from lag days −37 to −16 for the $SWI_1 > 1$ case. In the case of $SWI_1 < −1$, the stratospheric polar vortex is weaker than average at lag days −20 to −18 and again at lag days −6 to 0, and the AO index is found to be lower than average from lag days −24 to +3. The variability in the warm pool OLR index occurs on time scales that suggest a possible link to the MJO. Therefore, it is possible that the MJO drives the early signal seen in the sea ice (Yoo et al. 2013; Henderson et al. 2014), the stratospheric polar vortex (Garfinkel et al. 2012), and the AO (Zhou and Miller 2005), the latter of which may also be supported by previous studies that have linked MJO convection to the NAO (Cassou 2008; Lin et al. 2009). More specifically, for the positive (negative) SWI_1 case, the OLR anomalies seen at lag days −60 to −53 (lag days −40 to −31) are opposite in sign compared to the OLR anomalies seen at lag days −18 to +2 (−20 to +2), suggesting a time scale of about 50 to 90 days, roughly consistent with
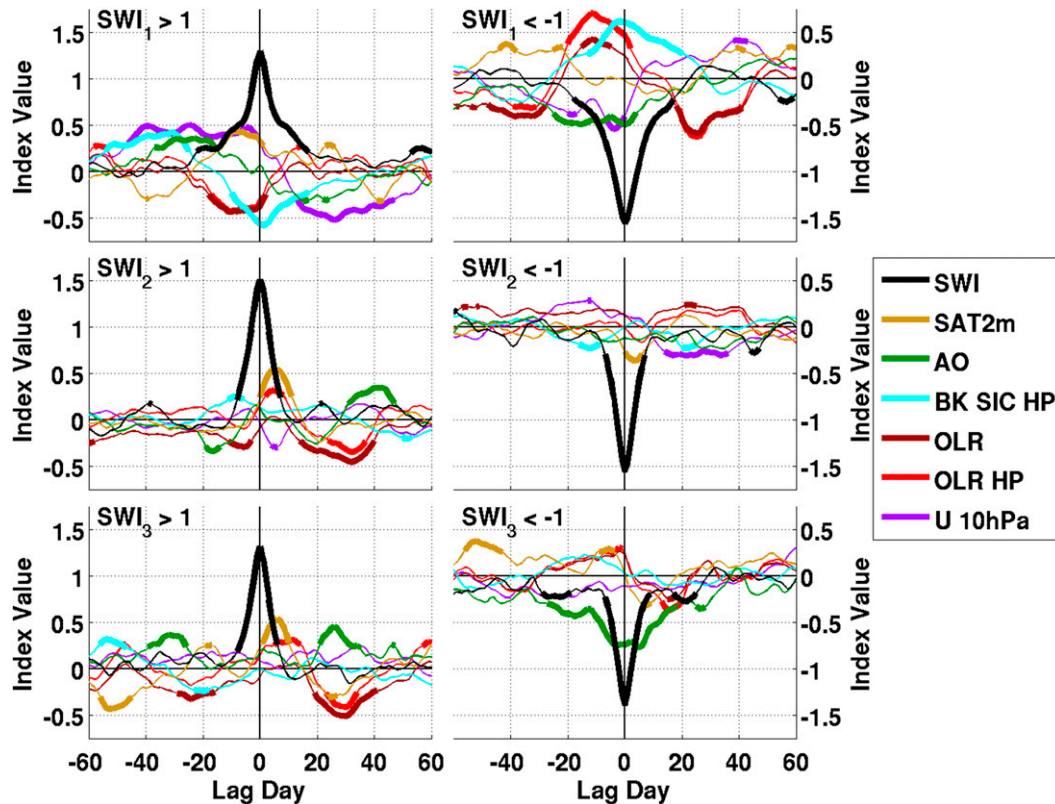
FIG. 9. Lagged composite plots of normalized indices, for DJF days with (left) constructive (index > 1.0) and (right) destructive (index < −1.0) interference. Composites are based on (top to bottom) SWI_1, SWI_2, and SWI_3 (see text). The line colors and thicknesses are as in Fig. 7, but the black curves correspond to (top to bottom) SWI_1, SWI_2, and SWI_3.

the MJO time scale. The early OLR anomalies peak before the anomalies seen in sea ice and the polar vortex at negative lags, suggesting the possibility of driving by the MJO.

To further test this relationship between the SWI_1 and the MJO, we have plotted lagged composites of the real-time multivariate MJO (RMM) indices of Wheeler and Hendon (2004) for times when $SWI_1 > 1.0$, and $SWI_1 < −1.0$, where the RMM1 and RMM2 indices are the principal component time series of the first two combined EOFs of 200- and 850-hPa zonal wind and OLR in the tropics (see Fig. 10). Thick solid lines at negative lags and thick dashed lines at positive lags indicate lag days for which the amplitude of the composite RMM1 and RMM2 indices is greater than the amplitude of randomly chosen RMM1 and RMM2 composites at the $p < 0.05$ level, according to a Monte Carlo simulation (here, amplitude is calculated as the square root of the sum of the squares of the composite RMM1 value and the composite RMM2 value). As with previous Monte Carlo simulations, the number of days that are randomly chosen for each composite is taken as the total number of composite days for each case divided by the

mean number of consecutive days for which the corresponding variable exceeds the threshold value. It is important to note here that we would not expect the amplitude of the RMM1 and RMM2 composites to be similar to a composite of daily MJO amplitudes, which are calculated as the square root of the sum of the squares of the RMM1 value and the RMM2 value for each day. This is because the distributions of RMM1 and RMM2 values each have a mean near zero, but the distribution of daily MJO amplitudes has a mean near 1.2. When the SWI_1 is positive, the composite MJO moves from phase 3 at lag day −23, through phase 5 near lag day −6, and all the way to phase 8 by lag day +23, having a statistically significant amplitude throughout [note that Wheeler and Hendon (2004) define eight phases for the MJO]. For the negative SWI_1 case, the MJO moves from the edge of phase 5 and 6 at lag day −33, through to phase 1 near lag day −6, and back around to phase 5 by lag day +33, with the only period lacking significance at the $p < 0.05$ level occurring from lag day −6 to lag day +3. The OLR and RMM1/RMM2 composite results support the hypothesis that warm pool convection associated with the MJO is partly
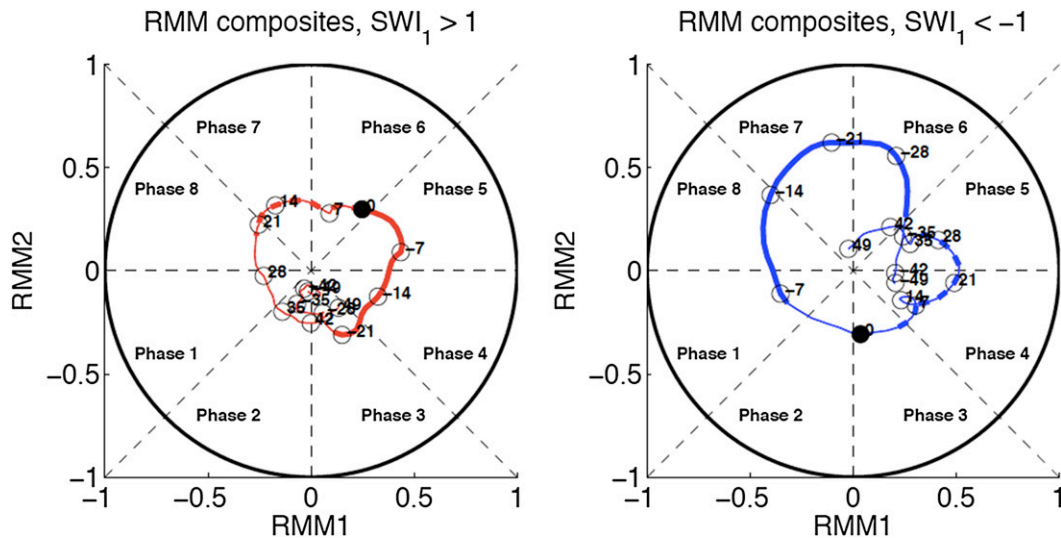
FIG. 10. Lagged composite plot of the RMM1 and RMM2 indices for DJF days with (left) $SWI_1 > 1.0$ and (right) $SWI_1 < -1.0$. Circles with labeled numbers show the lag day. The thick solid line at negative lags and the thick dashed line at positive lags correspond to times when the distance from the origin is significant at the $p < 0.05$ level, according to a Monte Carlo simulation (see text).

responsible for driving large Barents and Kara Sea ice concentration and stratospheric polar vortex anomalies at negative lags.

To examine if the relationship between positive SWI_1 and the deceleration of the stratospheric polar vortex, and vice versa for negative SWI_1, is associated with vertical wave activity propagation from the troposphere into the stratosphere, we calculate lagged composites of the meridional heat flux at 100 hPa. The results are shown in the top (bottom) panel of Fig. 11, calculated as $[v*T*]'$, where v is the meridional component of the wind at 100 hPa, T is the temperature at 100 hPa, the square brackets denote the zonal mean, an asterisk the deviation from the zonal mean, and a prime the deviation from the seasonal cycle (as defined earlier). Stippling indicates lag days and latitudes for which the top and bottom composites are different at the $p < 0.05$ level, based on a Monte Carlo simulation performed in the same manner as for Figs. 2–7 and 9. We see a signal for enhanced (suppressed) poleward heat flux at this level from lag days -1 to $+40$, peaking at lag days $+7$ to $+10$, and focused between latitudes $40°$ to $70°N$, for the constructive (destructive) interference case. This demonstrates that constructive (destructive) interference with the zonal wavenumber 1 component of the stationary wave leads to enhanced (suppressed) vertical wave activity propagation into the stratosphere for several weeks following the interference.

Additionally, we decompose the 100-hPa heat flux into three terms—that is, $[v*T*]' = [v'*\mathbf{T}*] + [\mathbf{v}*T'*] + [v'*T'*]$,

where boldface denotes the DJF time mean (not shown). The first term on the right-hand side of this equation closely matches the anomalous heat flux (the left-hand side). Together with our results in Fig. 10, these findings suggest that the vertical propagation of wave activity into the stratosphere, over a wide range of lags, arises from the interaction between the zonal wavenumber 1 transient eddy wind field triggered by MJO convection with the zonal wavenumber 1 climatological stationary eddy temperature field.

The results seen in Figs. 9 and 11 present a clean link between warm pool convective forcing, constructive interference, Arctic SAT, sea ice anomalies, the stratospheric polar vortex, and the AO. We suggest the following physical picture for the constructive interference case. First, enhanced warm pool convection forces a Rossby wave train that constructively interferes with the climatological stationary wave. The amplified stationary wave is associated with enhanced meridional flow, transporting heat and moisture into the Arctic. In response, the Arctic SAT increases, and sea ice concentrations in the Barents and Kara Seas become anomalously low. As demonstrated in Fig. 11, as well as discussed in studies such as Smith et al. (2011), enhanced wave activity associated with constructive interference with the stationary wave at low zonal wavenumbers propagates vertically into the stratosphere, disrupting the stratospheric polar vortex and weakening the stratospheric westerlies. This process occurs over longer time scales, ranging from weeks to months. Finally, the
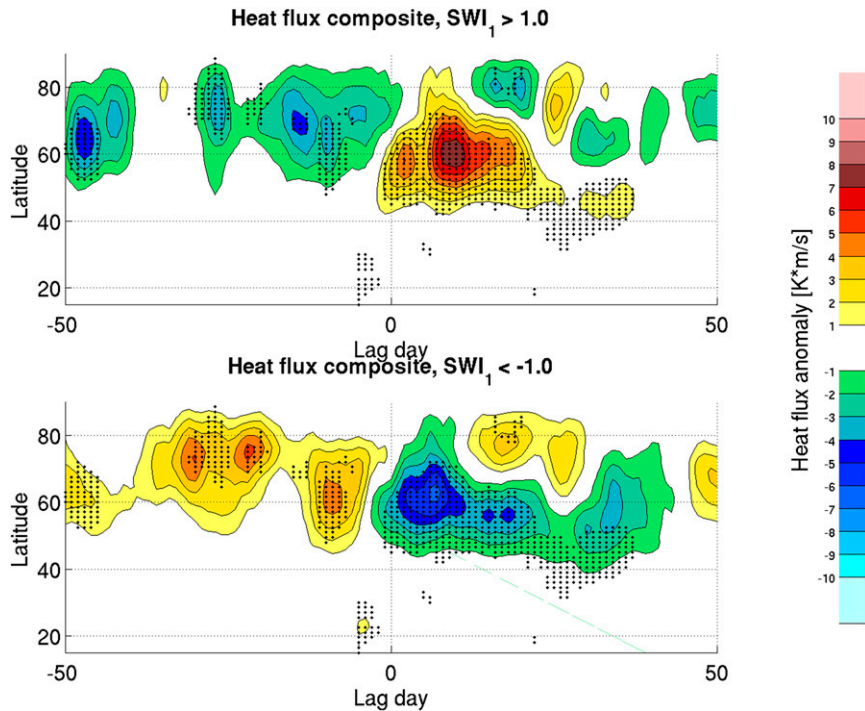
Heat flux composite, SWI₁ > 1.0

FIG. 11. Lag–latitude composite plot of the zonal mean heat flux anomaly $[v^*T^*]'$ at 100 hPa for DJF days with (top) $SWI_1 > 1.0$ (top) and (bottom) $SWI_1 < -1.0$. Stipples indicate latitudes and times for which the top and bottom composites differ at the $p < 0.05$ level, according to a Monte Carlo simulation (see text).

surface signal of the weakened stratospheric polar vortex occurs in the form of a more negative AO. A similar picture emerges for the destructive interference case but with the process reversed. Suppressed convection leads to a deamplification of the stationary wave, reducing the meridional flow and the heat and moisture transport into the Arctic, allowing the Barents and Kara Sea ice concentrations to increase and cooling the Arctic. Destructive interference with the wavenumber 1 stationary wave reduces the wave activity propagating into the stratosphere, allowing the polar vortex to strengthen, which finally increases the AO.

For both SWI_2 and SWI_3 in Fig. 9, enhanced warm pool convection precedes the peak of the constructive interference, and a warm Arctic SAT signal is seen near lag day +5. Following the peak in constructive interference for both zonal wavenumbers, the high-pass-filtered warm pool OLR is seen to increase, and then decrease again, which could be related to the MJO. There is also a positive AO signal 20 to 40 days following interference at both zonal wavenumbers 2 and 3. For both SWI_2 and SWI_3 destructive interference, a negative Arctic SAT signal is seen around lag day +5. For $-SWI_3$, we see a signal for a negative AO with a broad peak centered at lag day 0. Much of the variability seen in Fig. 7 is dominated by the zonal wavenumber 1

contribution, with the exception being the Arctic SAT variations at positive lags, which seem to be largely a consequence of interference with the zonal wavenumber 2 and 3 stationary wave and the associated convective anomalies at negative lags. The strong Arctic SAT response seen at wavenumber 2 is somewhat intuitive, as Fig. 4 suggests a wavenumber 2–like temperature field with two main regions of high-latitude heat transport— the first centered over the Barents and Kara Seas and the second centered over Alaska.

A histogram of DJF SWI values is displayed in Fig. 12. Each full bar represents the number of total days (the count) having an SWI value within a 0.5-wide bin. For each full bar, two more binning processes are carried out. First, the days are binned by warm pool convection, using the normalized version of the OLR index defined earlier. These bins are marked by the green (enhanced convection, index less than −0.5), black (neutral convection, index between −0.5 and 0.5), and gold (suppressed convection, index greater than 0.5) outlines and are based on the mean OLR index value between lag −10 and 0 days. The Arctic SAT index (defined earlier) is then used to bin each OLR bin, again with thresholds at ±0.5 standard deviations, and where the bins are based on the mean value of the SAT index
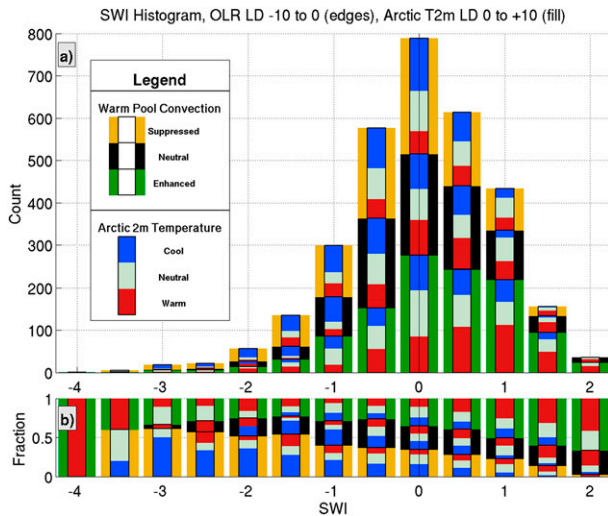
FIG. 12. (a) Histogram of the DJF SWI. SWI bins are 0.5 wide each, with a lower bound of −4.25 and an upper bound of +2.25. For each SWI bin, the outer vertical bar colors correspond to the three different lag −10 to 0 day warm pool OLR index bins. Anomalously strong warm pool convection (OLR index < −0.5) is marked by a green outer bar, neutral warm pool convection (−0.5 < OLR index < 0.5) by a black outer bar, and anomalously weak warm pool convection (OLR index > 0.5) by a gold outer bar. Also, for each SWI bin, the inner colors correspond to three different lag 0 to +10 day Arctic SAT index bins. An anomalously warm Arctic (Arctic SAT index > 0.5) is marked by a red inner bar, a neutral Arctic (−0.5 < Arctic SAT index < 0.5) by a pale green inner bar, and an anomalously cool Arctic (0.5 < Arctic SAT index) by a blue inner bar. (b) As in (a), but with bins plotted in reversed order and normalized by the amount of days in each SWI bin.

between lag days 0 and +10. Here, the red fill corresponds to a warm Arctic, the green corresponds to a neutral Arctic, and the blue corresponds to a cool Arctic. A version of the histogram based on the fraction of days in each SWI bin is shown in the bottom of the figure and is presented to more easily see the relationship between the SWI, suppressed convection, and cool Arctic temperatures.

Several relationships between the stationary wave interference, warm pool convection, and the Arctic SAT can be seen in Fig. 12. For example, we see that positive SWI values are associated with a greater frequency of enhanced warm pool convection, and vice versa for negative SWI values. A warm Arctic is also observed more frequently during times of positive SWI values, with a cool Arctic occurring more often during periods when the SWI is negative. Additionally, the association between the SWI and the Arctic SAT appears strongest when the warm pool convection signal is of the expected sign. That is, for a given SWI bin, the frequency of warm Arctic cases tends to be greater when warm pool convection is enhanced than when it is neutral or

suppressed. Likewise, for a given SWI bin, the frequency of cold Arctic cases tends to be greater when warm pool convection is suppressed than when it is neutral or enhanced. However, since the associations found in this study between warm pool convection, stationary wave interference, and Arctic temperatures are occasionally reversed, other physical mechanisms may also play a role. For example, interference may occasionally be driven by variability in the midlatitudes alone rather than having a source in warm pool convective forcing. Likewise, Arctic temperature anomalies may be the result of other processes, such as surface heat exchanges driven by anomalous sea ice, or meridional flow anomalies in quadrature with the climatological stationary wave.

Two additional versions of Fig. 12 are also produced using the Barents and Kara Sea ice index at lag days −45 to −35 and the 10-hPa zonal wind index at lag days −10 to 0 instead of using the OLR index at lag days −10 to 0. We calculate these plots in order to test the possibility that preconditioning from sea ice or the stratospheric polar vortex may affect the impact of interference on the Arctic SAT. The results are not shown here, but we find that the frequency of high (low) sea ice concentration anomalies in the Barents and Kara Seas is increased prior to +SWI (−SWI) days, consistent with the sign of the sea ice anomalies seen at negative lags in Fig. 7. Likewise, the frequency of strong (weak) stratospheric polar vortex anomalies is increased prior to +SWI (−SWI) days, consistent with the sign of 10-hPa zonal wind anomalies seen at negative lags in Fig. 7. The distribution of Arctic temperatures within a given SWI bin tends to be relatively insensitive to high, neutral, and low sea ice and likewise to high, neutral, and low polar vortex strength. This result suggests that, while the +SWI (−SWI) tends to be preceded by high (low) sea ice in the Barents and Kara Seas at long negative lags and by a stronger (weaker) than normal stratospheric polar vortex and shorter negative lags, indicating that preconditioning of stationary wave interference by these variables is a possibility, this potential preconditioning does not substantially affect the SAT response to interference.

To further investigate the link between warm pool convection, the stationary wave, and Arctic temperatures, we impose an additional condition on the composite calculation. Specifically, for both the constructive (SWI > 1.0) and destructive (SWI < −1.0) cases, we subdivide the composites into three categories based on the mean lag −10 to 0 day OLR index being either less than −0.5 (enhanced convection), between −0.5 and 0.5 (neutral convection), or greater than 0.5 (suppressed convection). In other words, we calculate composites

based on the subset of days outlined with green, black, and gold vertical bars in Fig. 12. This allows us to address the role of convection in altering Arctic temperatures in the presence of interference.

Figures 13 and 14 show lagged composites of the anomalous 2-m temperature when there is constructive and destructive interference, respectively. The left column corresponds to enhanced warm pool convection, the middle column to neutral warm pool convection, and the right column to suppressed warm pool convection, as defined above. Statistical significance, indicated by the stippling, is calculated using a Monte Carlo simulation as for Figs. 2–6, except that instead of testing whether the positive and negative SWI composites have different means using a Monte Carlo simulation, we test whether a composite for a single OLR bin is being drawn from a distribution that is different from the distribution associated with the other two OLR bins for the same sign of the SWI. In both Figs. 13 and 14, we see that the strongest local temperature anomalies appear as a dipole, with one center over Alaska and the other over northeastern North America, from lag days 0 through +6. The strongest anomalies are seen in the +SWI case with the positive OLR bin, and in the −SWI case with the negative OLR bin. In addition, we see in Fig. 13 that the warm Arctic SAT anomalies following times of constructive interference are most widespread and persistent when also preceded by enhanced warm pool convection. Specifically, at lag days +10 and +14, we see a statistically significant signal for a warm SAT at high latitudes for the −OLR composite, and for a neutral or cool high latitude SAT for the +OLR composites. Likewise, as seen in Fig. 14 for the −SWI case at the same lags, we see a statistically significant neutral to warm SAT signal over the East Siberian and Chukchi Seas for the −OLR composite, with a statistically significant cool SAT signal over the same region for the +OLR composite. This suggests that the Arctic response to interference with the climatological stationary wave is modulated substantially by anomalies at earlier lags in warm pool convection.

4. Conclusions

In this study, we used observation-based data to address questions related to 1) the structure and variability of the eddies associated with interference with the climatological stationary wave, 2) how interference relates to warm pool convection, 3) how interference relates to Arctic 2-m temperature, and 4) the sensitivity of the Arctic temperature/stationary wave interference relationship to tropical convection. To address these questions, an index, the SWI, was developed to characterize transient eddy interference with the Northern Hemispheric climatological stationary wave. This was done by projecting the daily 300-hPa streamfunction anomaly pattern onto the 300-hPa climatological stationary wave.

For the first question, we find that the amplitude of the anomalous wave field when interference takes place is largest during DJF. The spatial structure of this wave field does not change much between the autumn and spring seasons but differs substantially in the summer, during which only very weak composite anomalies are present. Outside of summer, we see that constructive interference is associated with a more amplified climatological stationary wave, while during times of destructive interference, the composite 300-hPa streamfunction pattern is nearly zonal.

In response to the second question, a close association between tropical convection and the climatological stationary wave is found. More specifically, constructive interference with the stationary wave is preceded, at lags of about one week, by enhanced convection over the warm pool region. Likewise, destructive interference is preceded by suppressed convection over the warm pool region.

With regard to the third question, we find a significant relationship between transient eddy interference with the climatological stationary wave and Arctic 2-m temperature. Specifically, following constructive interference, warm anomalies spread over the Arctic. Destructive interference is followed by cold anomalies throughout much of the Arctic. These results are somewhat intuitive, in that constructive interference is associated with a large-amplitude wave field and thus a stronger meridional flow, allowing warm, moisture-laden air to penetrate high latitudes. This occurs most prominently in two regions, one over Alaska and the Bering Strait and the other over northern Russia and the Barents and Kara Seas, which is also associated with a reduction in sea ice over this region. When there is destructive interference, the flow is more zonally oriented and cold air is trapped over the polar region.

To respond to the fourth question, a histogram was created to visualize the frequency of enhanced, neutral, and suppressed warm pool convection, as well as the frequency of a warm, neutral, and cool Arctic, based on the value of the SWI, representing transient eddy interference with the climatological stationary wave. We find that the state of the tropical warm pool convection does modulate the Arctic surface temperature response to interference; that is, when both enhanced convection and constructive interference are present, the Arctic is warm more frequently than when constructive interference is present without enhanced warm pool
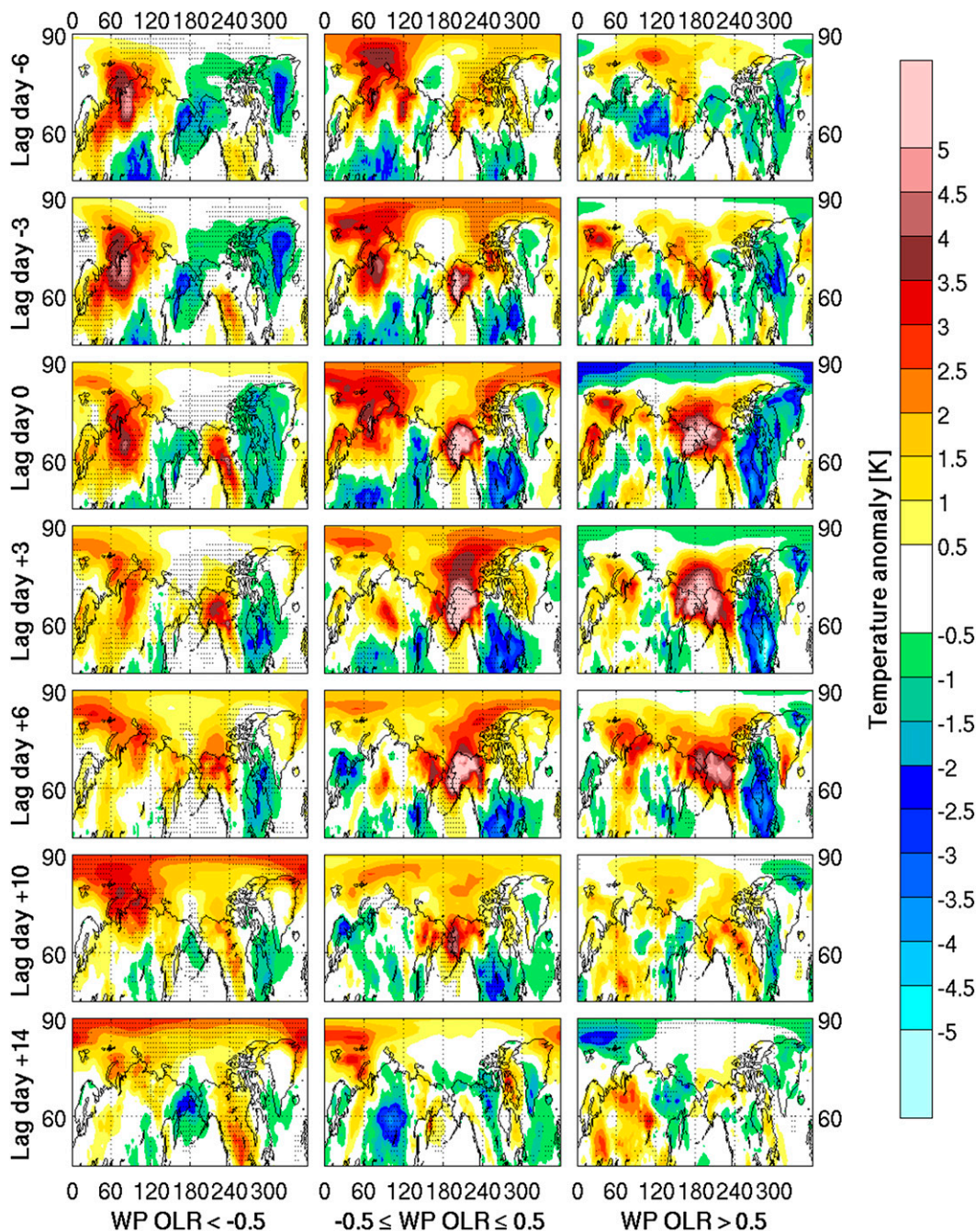
Fig. 13. Lagged composite anomalous 2-m temperature maps for DJF days with SWI > 1.0 and for which the lag −10 to 0 day OLR index value is (left) less than −0.5 (enhanced warm pool convection), (middle) between −0.5 and +0.5 (warm pool convection), or (right) greater than 0.5 (weak warm pool convection). The rows correspond to (top to bottom) lag −6, −3, 0, +3, +6, +10, and +14 days. Stippling indicates regions where the composites are statistically different from days in the other two convective bins with SWI > 1.0 at the $p < 0.05$ level, according to a Monte Carlo simulation (see text for details).

convection. Likewise, when both suppressed convection and destructive interference are present, the Arctic tends to be cool more frequently than when destructive interference exists without suppressed warm pool

convection. The results related to the second, third, and fourth questions suggest a possible mechanism by which the tropically excited Arctic warming (TEAM) mechanism (Lee et al. 2011a) may occur; that is, enhanced
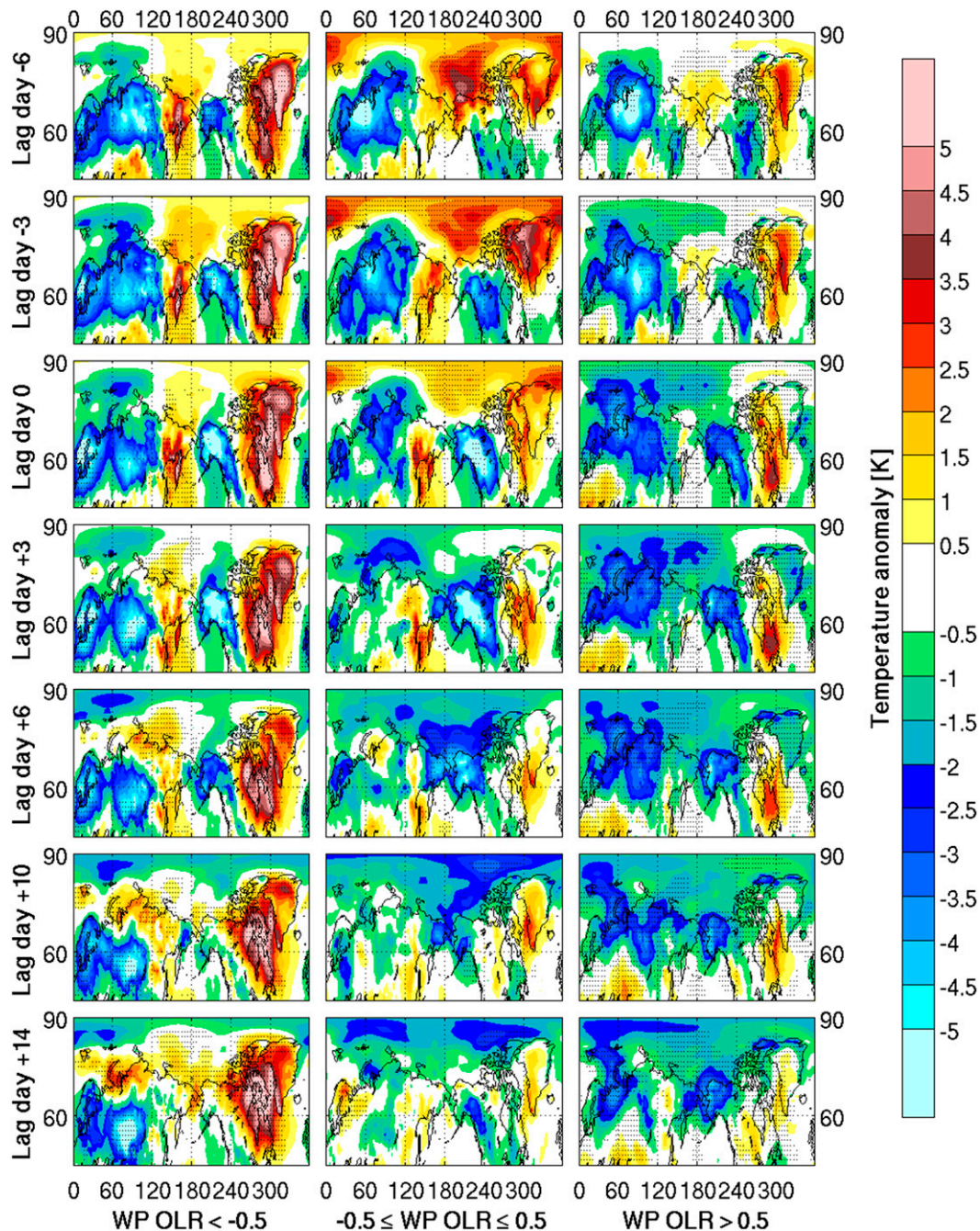
FIG. 14. As in Fig. 13, but for DJF days with SWI < −1.0.

warm pool convection can lead to a larger-amplitude midlatitude wave field through interference, which in turn increases the meridional flow and forces warm, moist air into the Arctic, warming the surface. The reverse happens when convection is suppressed over the warm pool region.

This study has potential implications with regard to climate change, depending on how tropical convection is likely to change in a global warming scenario. If, for example, equatorial sea surface temperatures increase equally at all longitudes, then, because of the exponential relationship between temperature and saturation vapor pressure (the Clausius–Clapeyron relationship), one would expect zonal convective perturbations to become even more localized and locally intense, resembling the "enhanced" warm pool convection case

([Lee et al. 2011a](#)). In this scenario, one would expect stronger constructive interference, which might provide a catalyst for further Arctic warming.

REFERENCES

Baggett, C., and S. Lee, 2015: Arctic warming induced by tropically forced tapping of available potential energy and the role of the planetary-scale waves. *J. Atmos. Sci.*, **72**, 1562–1568, doi:10.1175/JAS-D-14-0334.1.

Baldwin, M. P., and T. J. Dunkerton, 1999: Propagation of the Arctic Oscillation from the stratosphere to the troposphere. *J. Geophys. Res.*, **104**, 30 937–30 946, doi:10.1029/1999JD900445.

——, and ——, 2001: Stratospheric harbingers of anomalous weather regimes. *Science*, **294**, 581–584, doi:10.1126/science.1063315.

Cassou, C., 2008: Intraseasonal interaction between the Madden–Julian oscillation and the North Atlantic Oscillation. *Nature*, **455**, 523–527, doi:10.1038/nature07286.

Charlton, A. J., A. O'Neill, D. B. Stephenson, W. A. Lahoz, and M. P. Baldwin, 2003: Can knowledge of the state of the stratosphere be used to improve statistical forecasts of the troposphere? *Quart. J. Roy. Meteor. Soc.*, **129**, 3205–3225, doi:10.1256/qj.02.232.

Cohen, J., and J. Jones, 2011: Tropospheric precursors and stratospheric warmings. *J. Climate*, **24**, 6562–6572, doi:10.1175/2011JCLI4160.1.

——, M. Barlow, P. J. Kushner, and K. Saito, 2007: Stratosphere–troposphere coupling and links with Eurasian land surface variability. *J. Climate*, **20**, 5335–5343, doi:10.1175/2007JCLI1725.1.

——, J. C. Furtado, J. Jones, M. Barlow, D. Whittleston, and D. Entekhabi, 2014: Linking Siberian snow cover to precursors of stratospheric variability. *J. Climate*, **27**, 5422–5432, doi:10.1175/JCLI-D-13-00779.1.

Ding, Q., J. M. Wallace, D. S. Battisti, E. J. Steig, A. J. E. Gallant, H.-J. Kim, and L. Geng, 2014: Tropical forcing of the recent rapid Arctic warming in northeastern Canada and Greenland. *Nature*, **509**, 209–212, doi:10.1038/nature13260.

Feldstein, S., and S. Lee, 2014: Intraseasonal and interdecadal jet shifts in the Northern Hemisphere: The role of warm pool tropical convection and sea ice. *J. Climate*, **27**, 6497–6518, doi:10.1175/JCLI-D-14-00057.1.

Fletcher, C. G., and P. J. Kushner, 2011: The role of linear interference in the annular mode response to tropical SST forcing. *J. Climate*, **24**, 778–794, doi:10.1175/2010JCLI3735.1.

Garfinkel, C. I., D. L. Hartmann, and F. Sassi, 2010: Tropical precursors of anomalous Northern Hemisphere stratospheric polar vortices. *J. Climate*, **23**, 3282–3299, doi:10.1175/2010JCLI3010.1.

——, S. B. Feldstein, D. W. Waugh, C. Yoo, and S. Lee, 2012: Observed connection between stratospheric sudden warmings and the Madden-Julian oscillation. *Geophys. Res. Lett.*, **39**, L18807, doi:10.1029/2012GL053144.

Gillett, N. P., M. P. Baldwin, and M. R. Allen, 2001: Evidence for nonlinearity in observed stratospheric circulation changes. *J. Geophys. Res.*, **106**, 7891–7902, doi:10.1029/2000JD900720.

Held, I. M., M. Ting, and H. Wang, 2002: Northern winter stationary waves: Theory and modeling. *J. Climate*, **15**, 2125–2144, doi:10.1175/1520-0442(2002)015<2125:NWSWTA>2.0.CO;2.

Henderson, G. R., B. S. Barrett, and D. M. Lafleur, 2014: Arctic sea ice and the Madden–Julian oscillation (MJO). *Climate Dyn.*, **43**, 2185–2196, doi:10.1007/s00382-013-2043-y.

Hoskins, B. J., and D. J. Karoly, 1981: The steady linear response of a spherical atmosphere to thermal and orographic forcing. *J. Atmos. Sci.*, **38**, 1179–1196, doi:10.1175/1520-0469(1981)038<1179:TSLROA>2.0.CO;2.

Kim, B.-M., S.-W. Son, S.-K. Min, J.-H. Jeong, S.-J. Kim, X. Zhang, T. Shim, and J.-H. Yoon, 2014: Weakening of the stratospheric polar vortex by Arctic sea-ice loss. *Nat. Commun.*, **5**, 4646, doi:10.1038/ncomms5646.

Lee, S., 2012: Testing of the tropically excited Arctic warming (TEAM) mechanism with traditional El Niño and La Niña. *J. Climate*, **25**, 4015–4022, doi:10.1175/JCLI-D-12-00055.1.

——, 2014: A theory for polar amplification from a general circulation perspective. *Asia-Pac. J. Atmos. Sci.*, **50**, 31–43, doi:10.1007/s13143-014-0024-7.

——, T. T. Gong, N. C. Johnson, S. B. Feldstein, and D. Pollard, 2011a: On the possible link between tropical convection and the Northern Hemisphere Arctic surface air temperature change between 1958 and 2001. *J. Climate*, **24**, 4350–4367, doi:10.1175/2011JCLI4003.1.

——, S. B. Feldstein, D. Pollard, and T. S. White, 2011b: Do planetary wave dynamics contribute to equable climates? *J. Climate*, **24**, 2391–2404, doi:10.1175/2011JCLI3825.1.

Limpasuvan, V., and D. L. Hartmann, 2000: Wave-maintained annular modes of climate variability. *J. Climate*, **13**, 4414–4429, doi:10.1175/1520-0442(2000)013<4414:WMAMOC>2.0.CO;2.

Lin, H., G. Brunet, and J. Derome, 2009: An observed connection between the North Atlantic Oscillation and the Madden–Julian oscillation. *J. Climate*, **22**, 364–380, doi:10.1175/2008JCLI2515.1.

Park, D.-S., S. Lee, and S. B. Feldstein, 2015: Attribution of the recent winter sea ice decline over the Atlantic sector of the Arctic Ocean. *J. Climate*, **28**, 4027–4033, doi:10.1175/JCLI-D-15-0042.1.

Peings, Y., and G. Magnusdottir, 2014: Response of the wintertime Northern Hemisphere atmospheric circulation to current and projected Arctic sea ice decline: A numerical study with CAM5. *J. Climate*, **27**, 244–264, doi:10.1175/JCLI-D-13-00272.1.

Sardeshmukh, P. D., and B. J. Hoskins, 1988: The generation of global rotational flow by steady idealized tropical divergence. *J. Atmos. Sci.*, **45**, 1228–1251, doi:10.1175/1520-0469(1988)045<1228:TGOGRF>2.0.CO;2.

Simmons, A. J., 1982: The forcing of stationary wave motion by tropical diabatic heating. *Quart. J. Roy. Meteor. Soc.*, **108**, 503–534, doi:10.1002/qj.49710845703.

Smith, K. L., P. J. Kushner, and J. Cohen, 2011: The role of linear interference in northern annular mode variability associated with Eurasian snow cover extent. *J. Climate*, **24**, 6185–6202, doi:10.1175/JCLI-D-11-00055.1.

Thompson, D. W. J., M. P. Baldwin, and J. M. Wallace, 2002: Stratospheric connection to Northern Hemisphere wintertime weather: Implications for prediction. *J. Climate*, **15**, 1421–1428, doi:10.1175/1520-0442(2002)015<1421:SCTNHW>2.0.CO;2.

Wheeler, M. C., and H. H. Hendon, 2004: An all-season real-time multivariate MJO index: Development of an index for monitoring and prediction. *Mon. Wea. Rev.*, **132**, 1917–1932, doi:10.1175/1520-0493(2004)132<1917:AARMMI>2.0.CO;2.

Yoo, C., S. Lee, and S. B. Feldstein, 2012a: Mechanisms of extratropical surface air temperature change in response to the Madden–Julian oscillation. *J. Climate*, **25**, 5777–5790, doi:10.1175/JCLI-D-11-00566.1.

——, ——, and ——, 2012b: Arctic response to an MJO-like tropical heating in an idealized GCM. *J. Atmos. Sci.*, **69**, 2379–2393, doi:10.1175/JAS-D-11-0261.1.

——, S. B. Feldstein, and S. Lee, 2013: The prominence of a tropical convective signal in the wintertime Arctic temperature. *Atmos. Sci. Lett.*, **15**, 7–12, doi:10.1002/asl2.455.

Zhou, S., and A. J. Miller, 2005: The interaction of the Madden–Julian oscillation and the Arctic Oscillation. *J. Climate*, **18**, 143–159, doi:10.1175/JCLI3251.1.